Supplementary Information

Effects of surface hydrophobization on the phase evolution behavior of iron-based catalyst during Fischer–Tropsch synthesis

Yanfei Xu[1,2,*], Zhenxuan Zhang[1], Ke Wu[1], Jungang Wang[3], Bo Hou[3], Ruoting Shan[1], Ling Li[1], Mingyue Ding[1,4,*]

[1]School of Power and Mechanical Engineering, Wuhan University, Wuhan 430072, China

[2]Suzhou Institute of Wuhan University, Suzhou 215125, China

[3]State Key Laboratory of Coal Conversion, Institute of Coal Chemistry, Chinese Academy of Sciences, Taiyuan 030001, China

[4]Academy of Advanced Interdisciplinary Studies, Wuhan University, Wuhan 430072, China

*Corresponding author

E-mail address: yanfei_xu@whu.edu.cn (Yanfei Xu), dingmy@whu.edu.cn (Mingyue Ding).

Table of Contents

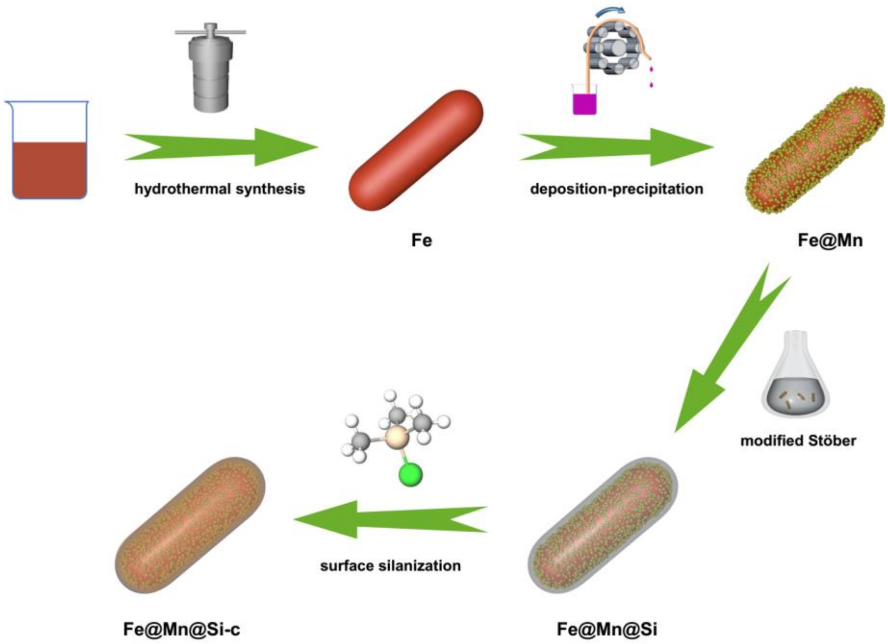

Supplementary Fig. 1. Synthesis steps of the hydrophilic and hydrophobic catalysts.

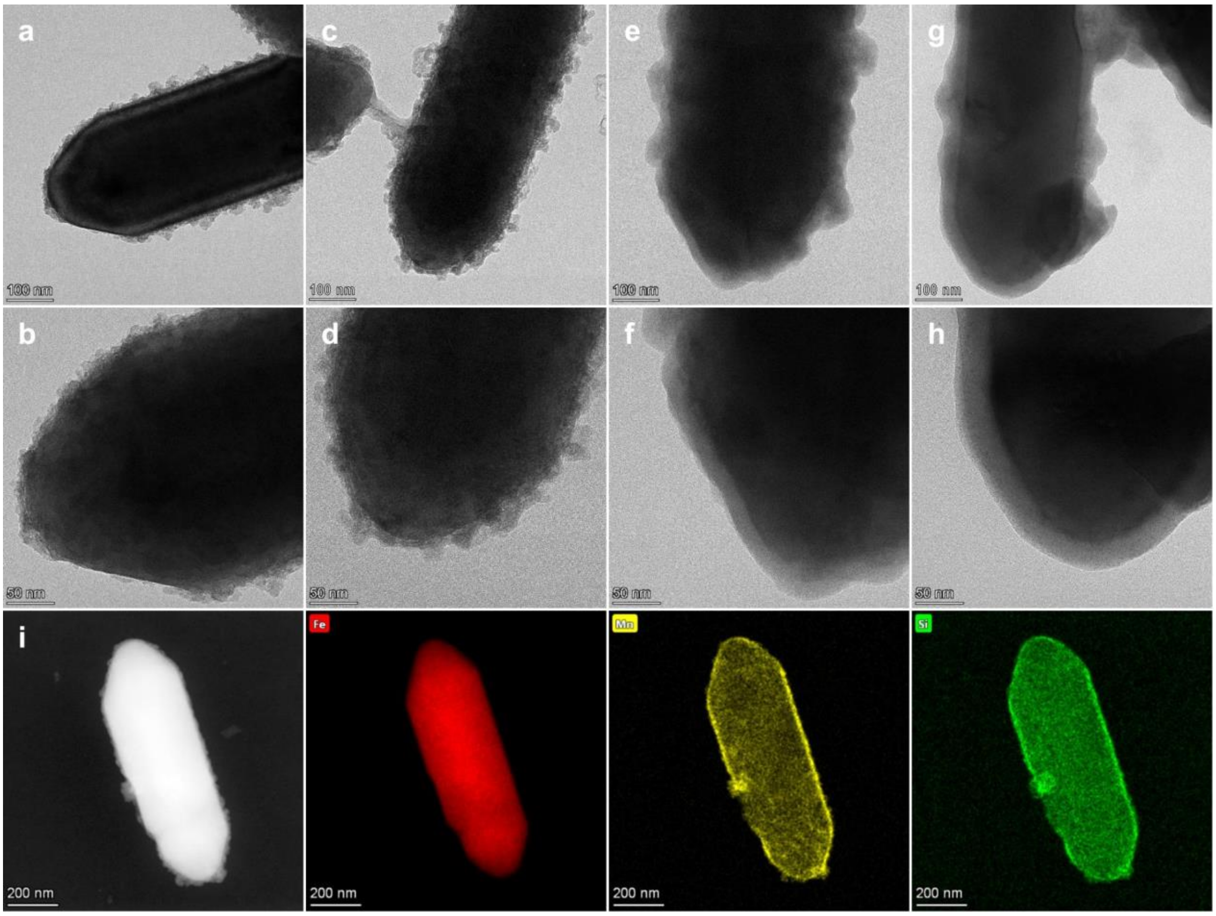

Supplementary Fig. 2. TEM images of (a,b) Fe@Mn@0.05Si, (c,d) Fe@Mn@0.2Si, (e,f) Fe@Mn@0.5Si, (g,h) Fe@Mn@2.8Si. (i) HAADF-TEM image and EDS elemental mapping of Fe@Mn@0.2Si.

The spatial distribution of Fe, Mn and Si elements in the Fe@Mn@0.2Si catalyst was revealed by the TEM-EDS elemental mapping. The Mn element was mainly located outside Fe element, confirming the coverage of MnO_2 on Fe_2O_3 surface. The Si element possessed the largest distribution region and was homogeneous in the catalyst, suggesting that the SiO_2 shell was uniformly coated on Fe@Mn nanoparticle. Besides, the SiO_2 shell gradually thickened with the increase of TEOS addition.

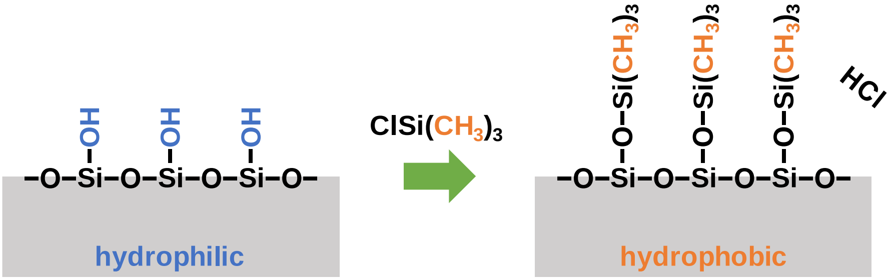

Supplementary Fig. 3. Hydrophobic modification via the surface silanization treatment.

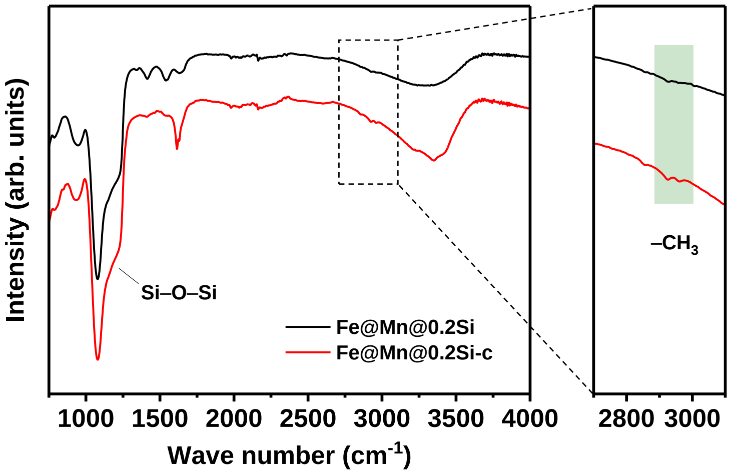

Supplementary Fig. 4. FTIR spectra of catalysts.

After the surface silanization treatment, new absorption bands at ~2925 cm^{-1} were detected on the spectrum of Fe@Mn@0.2Si-c catalyst, confirming the successful introduction of $-CH_3$ groups on catalyst surface.

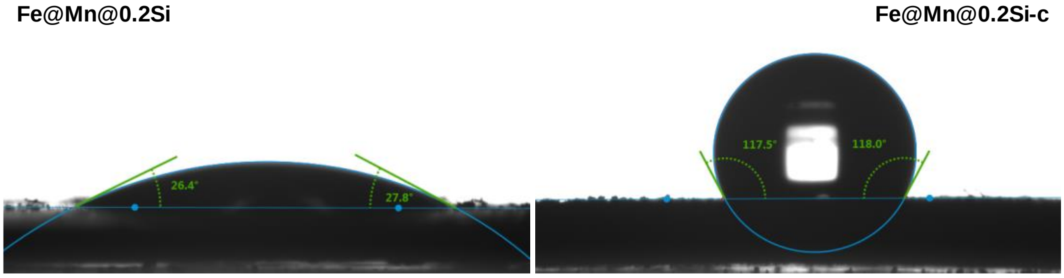

Supplementary Fig. 5. Water-droplet contact angle tests of catalysts.

The Fe@Mn@0.2Si catalyst possessed a hydrophilic surface with a water contact angle of 27 °. After the introduction of nonpolar $-CH_3$ groups via the surface silanization treatment, the obtained Fe@Mn@0.2Si-c catalyst exhibited good hydrophobicity with a water contact angle of 118 °.

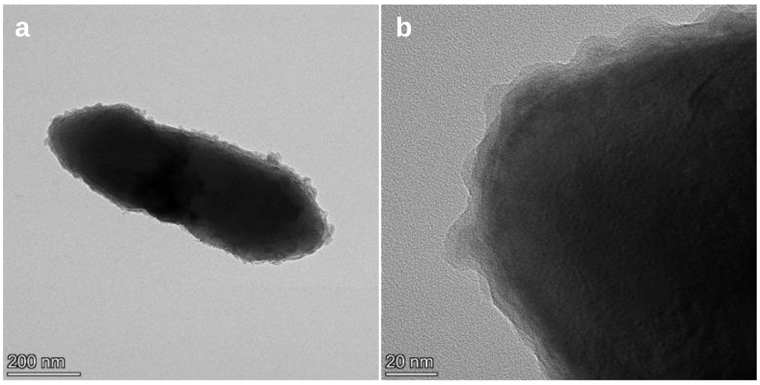

Supplementary Fig. 6. TEM images of the Fe@Mn@0.2Si-c catalyst.

The silanization reaction was proceeded on catalyst surface (Supplementary Fig. 3) and had no obvious influence on the thickness of SiO_2 shell.

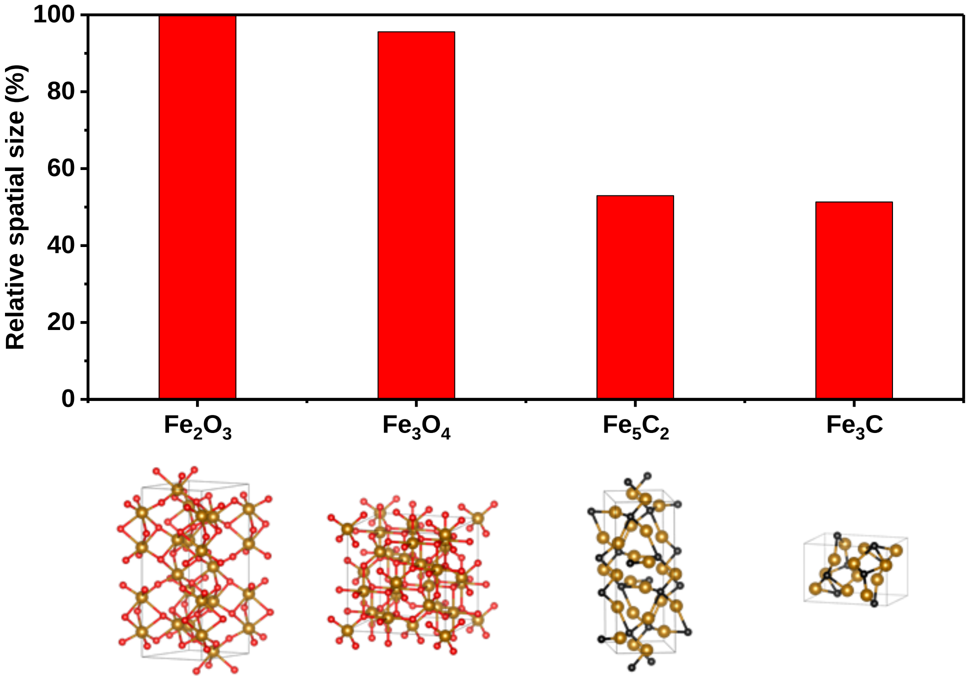

Supplementary Fig. 7. Relative spatial size of different iron phases.

The relative spatial size of different iron phases was calculated based on the volume of unit cell. First, the volume of each iron phase with 120 Fe atoms was calculated. Then, the volume ratios of different iron phases to Fe_2O_3 phase with the same number of Fe atoms were calculated. Detailed data were shown in Supplementary Table 2. The order of the relative spatial size of different iron phases is $Fe_2O_3 > Fe_3O_4 > Fe_5C_2 > Fe_3C$, implying that the reduction of Fe_2O_3 to Fe_3O_4 and carbonization of Fe_3O_4 to iron carbides (Fe_5C_2 and Fe_3C) are volume-decreasing processes.

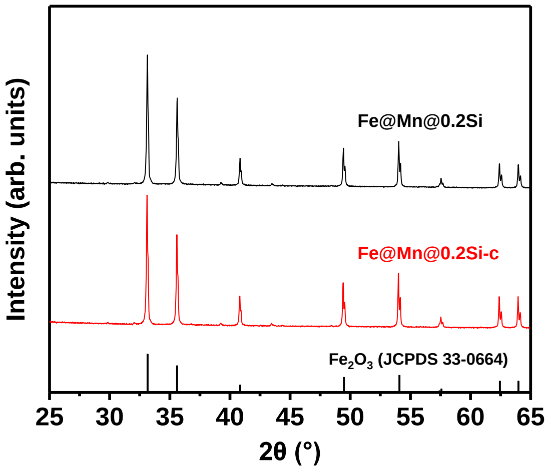

Supplementary Fig. 8. XRD patterns of catalysts.

Both of the fresh Fe@Mn@0.2Si and Fe@Mn@0.2Si-c catalysts were presented in the form of Fe_2O_3 phase.

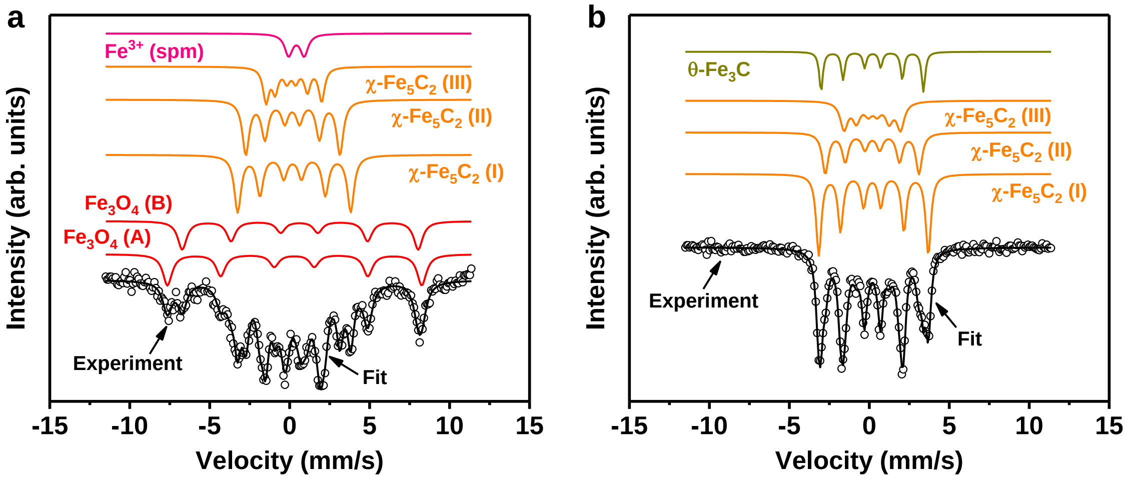

Supplementary Fig. 9. Mössbauer spectra of the (a) spent Fe@Mn@0.2Si and (b) spent Fe@Mn@0.2Si-c catalysts.

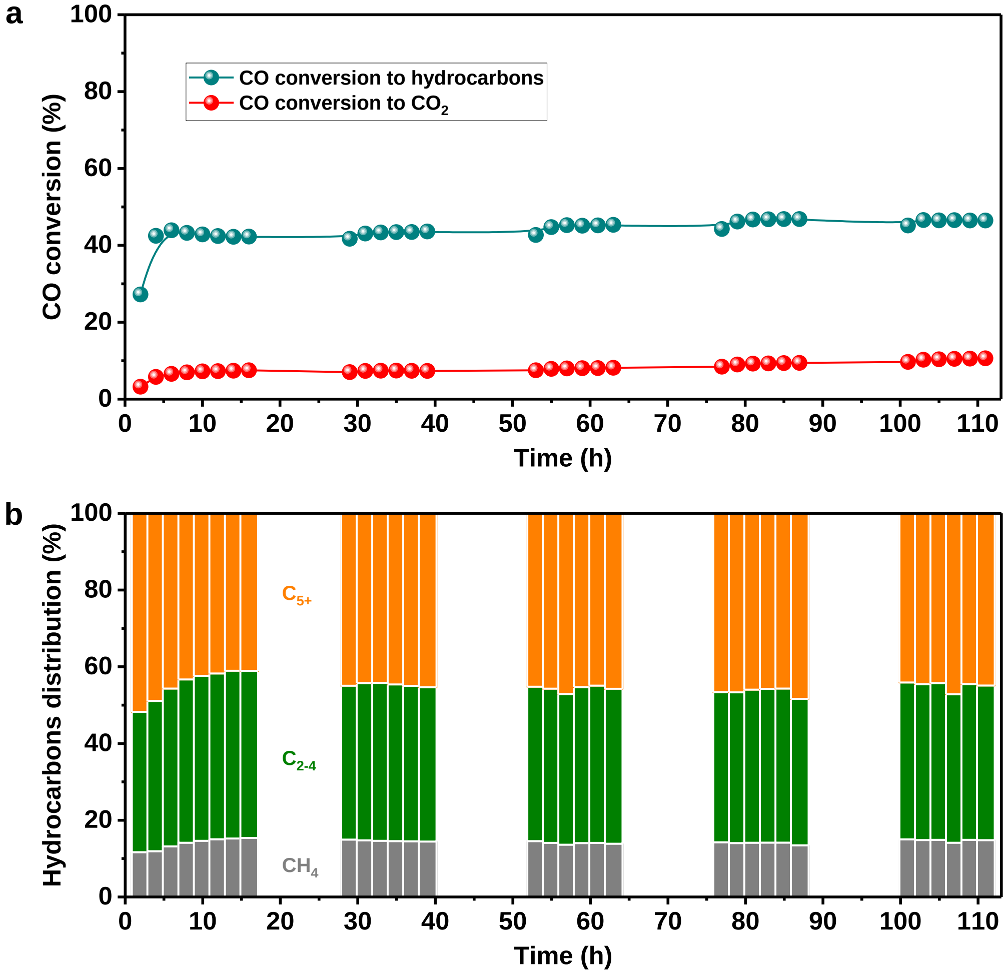

Supplementary Fig. 10. (a) CO conversion and (b) hydrocarbons distribution during the stability test of the Fe@Mn@0.2Si-c catalyst. The reaction data corresponding to the blank space in the figure was not collected, because the gas chromatograph was switched to another reactor at this time.

The Fe@Mn@0.2Si-c catalyst rapidly reached a relatively stable state within 4 hours. Besides, during 110 hours of continuous reaction, the CO conversion to hydrocarbons and CO_2 on this catalyst remained at about 45% and 8%, respectively. Meanwhile, the selectivity for CH_4 in hydrocarbons was stable at around 14%. These results suggested that the hydrophobic Fe@Mn@0.2Si-c catalyst possessed a good catalytic stability.

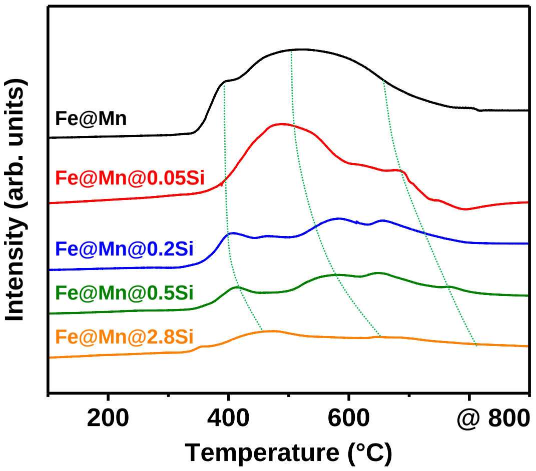

Supplementary Fig. 11. CO-TPR profiles of catalysts.

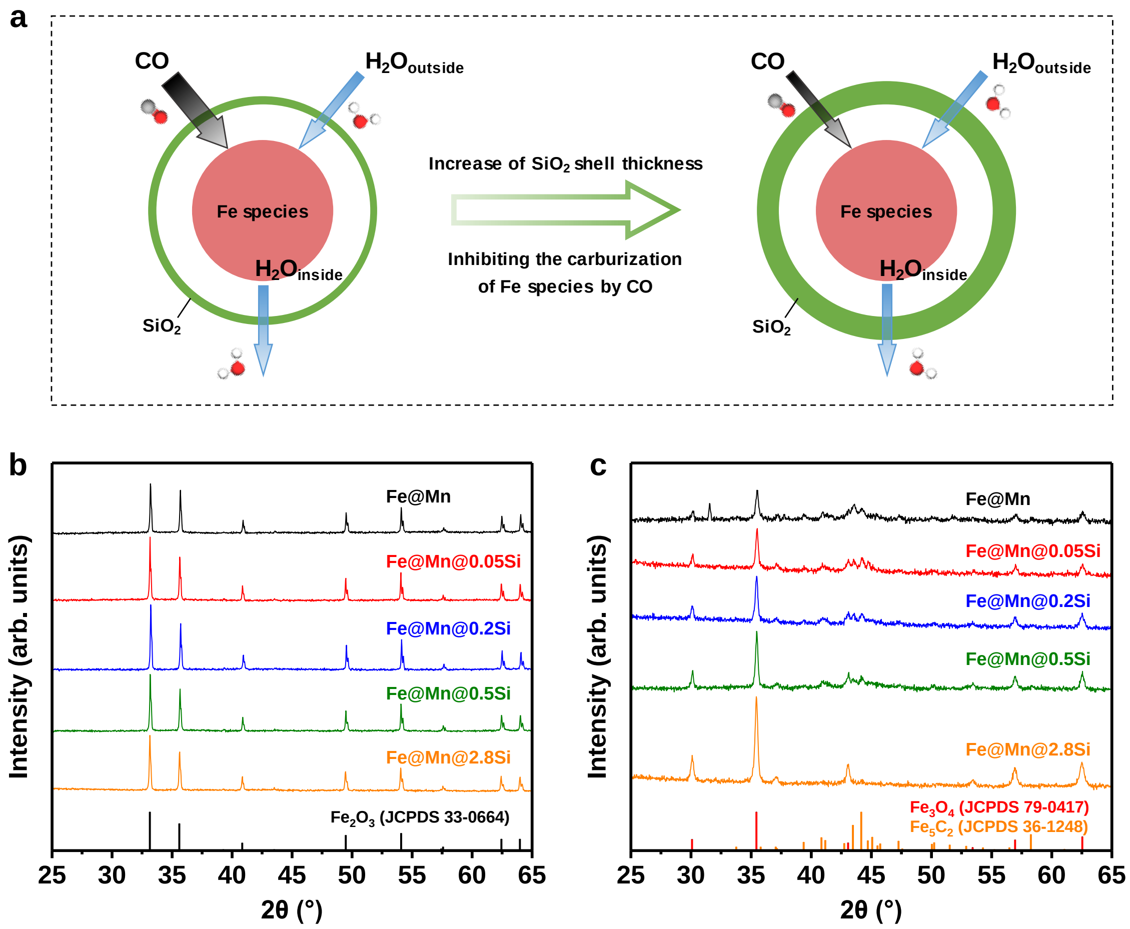

Supplementary Fig. 12. (a) Diffusion model of CO and H_2O on the hydrophilic catalysts during the FTS reaction. XRD patterns of the (b) fresh and (c) spent catalysts.

All of the fresh Fe@Mn@*x*Si catalysts were consisted of Fe_2O_3 phase. After the FTS reaction, the Fe_2O_3 in catalysts was transformed into a mixture of Fe_5C_2 and Fe_3O_4 phases. The increase of SiO_2 shell thickness could inhibit the accessibility and carburization of internal Fe species by CO molecules. Thus, with the thickening of SiO_2 shell, the intensity of diffraction peaks related to Fe_5C_2 phase gradually decreased, while that related to Fe_3O_4 phase obviously increased.

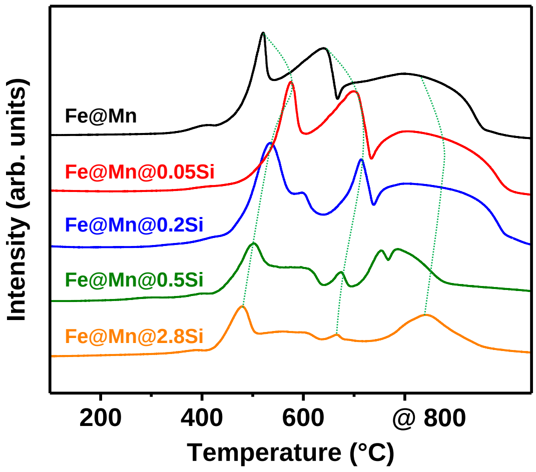

Supplementary Fig. 13. H_2-TPR profiles of catalysts.

After coating a small amount of SiO_2 (Fe@Mn@0.05Si), the reduction peaks of Fe_2O_3 shifted towards higher temperature, suggesting that the contact of metal with SiO_2 suppressed slightly its reduction, which was related to the metal-support interaction[1]. With the further thickening of SiO_2 shell, the reduction peaks shifted towards lower temperature, which may be attributed to that the micropores in shell could adsorb and enrich H_2[2,3] and thus promote the reduction of Fe_2O_3. These results suggested that the increase of SiO_2 shell thickness did not inhibit the accessibility and reduction of internal metal by H_2 molecules.

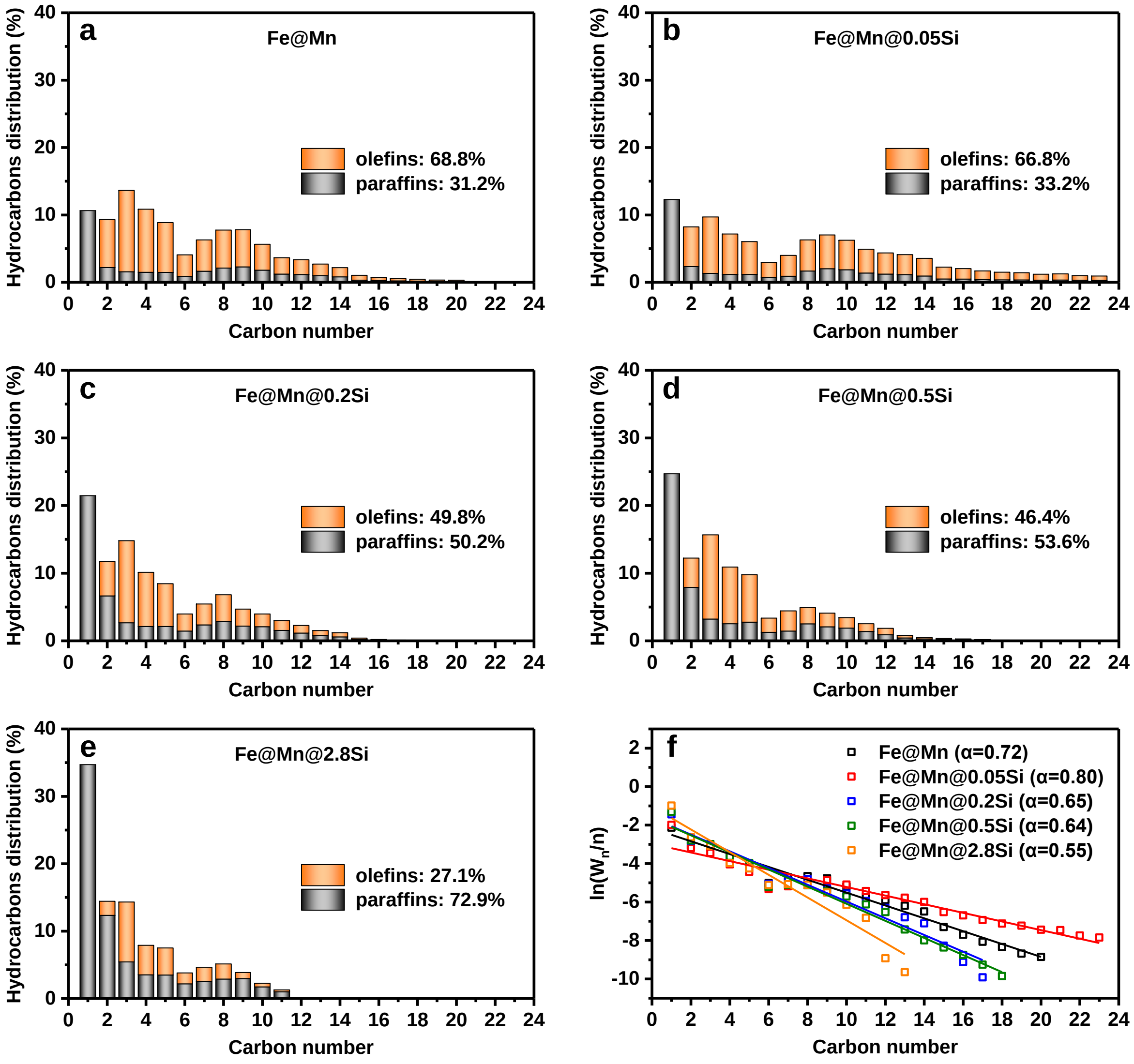

Supplementary Fig. 14. Hydrocarbons distribution of the (a) Fe@Mn, (b) Fe@Mn@0.05Si, (c) Fe@Mn@0.2Si, (d) Fe@Mn@0.5Si, and (e) Fe@Mn@2.8Si catalysts. (f) The ASF plots and relevant chain growth probability (α value) of the Fe@Mn@*x*Si catalysts.

Fe_xC phase was the active site for the C−C coupling process during FTS. Thus, with the increase of SiO_2 shell thickness, the α value (chain growth probability) decreased obviously from 0.80 to 0.55.

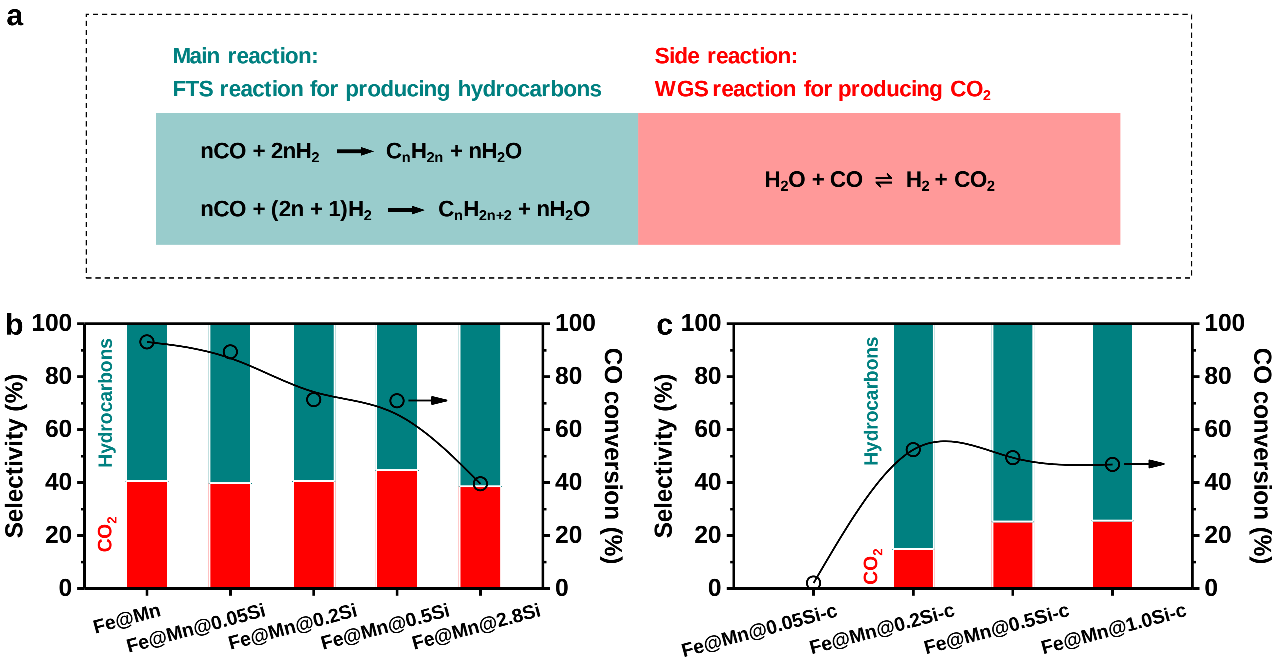

Supplementary Fig. 15. (a) Reactions occurring in the conversion of syngas. CO conversion and products distribution of the (b) Fe@Mn@*x*Si and (c) Fe@Mn@*x*Si-c catalysts.

Because water easily adsorbed on the hydrophilic Fe@Mn@*x*Si catalysts, serious WGS side reaction occurred and all the Fe@Mn@*x*Si catalysts exhibited high CO_2 selectivity of about 40%. This was also reflected from Supplementary Fig. 16, in which the CO_2 selectivity on the Fe@Mn@0.2Si catalyst was as high as 37~42% at CO conversion of 43~71%. The hydrophobic SiO_2 shell could reduce the water concentration in the core vicinity of catalyst, thereby suppressing the WGS side reaction. As a result, the hydrophobic Fe@Mn@*x*Si-c catalysts exhibited much lower CO_2 selectivity than the hydrophilic Fe@Mn@*x*Si catalysts. However, the increase of shell thickness inhibited the accessibility and carburization process of internal iron species by CO molecules, leading to the slight oxidation of iron species before water diffused outside the Fe@Mn@0.5Si-c and Fe@Mn@1.0Si-c catalysts (Supplementary Fig. 17c). As Fe_3O_4 phase is very active for the WGS reaction, the CO_2 selectivity on the Fe@Mn@*x*Si-c catalysts increased with the increase of shell thickness.

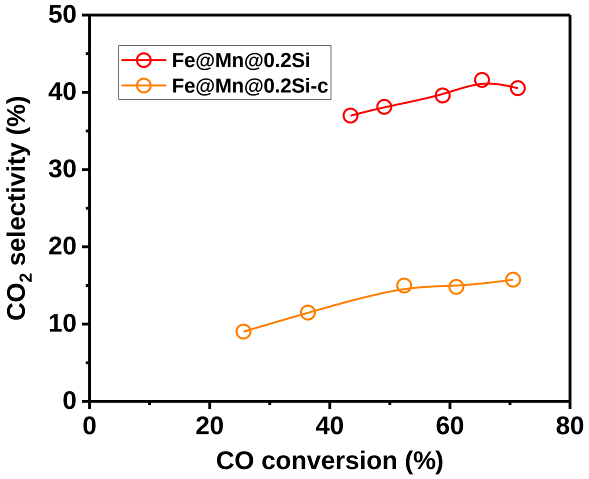

Supplementary Fig. 16. The CO_2 selectivity on the Fe@Mn@0.2Si and Fe@Mn@0.2Si-c catalysts at different CO conversion levels obtained by adjusting the space velocity. Reaction conditions: 320 ℃, 2.0 MPa, H_2/CO = 2.

At a series of CO conversion levels, the CO_2 selectivity on the Fe@Mn@0.2Si-c catalyst was much lower than that on the Fe@Mn@0.2Si catalyst, suggesting that the hydrophobic surface could inhibit effectively the participation of water in the WGS side reaction and suppress the production of undesired CO_2 by-product.

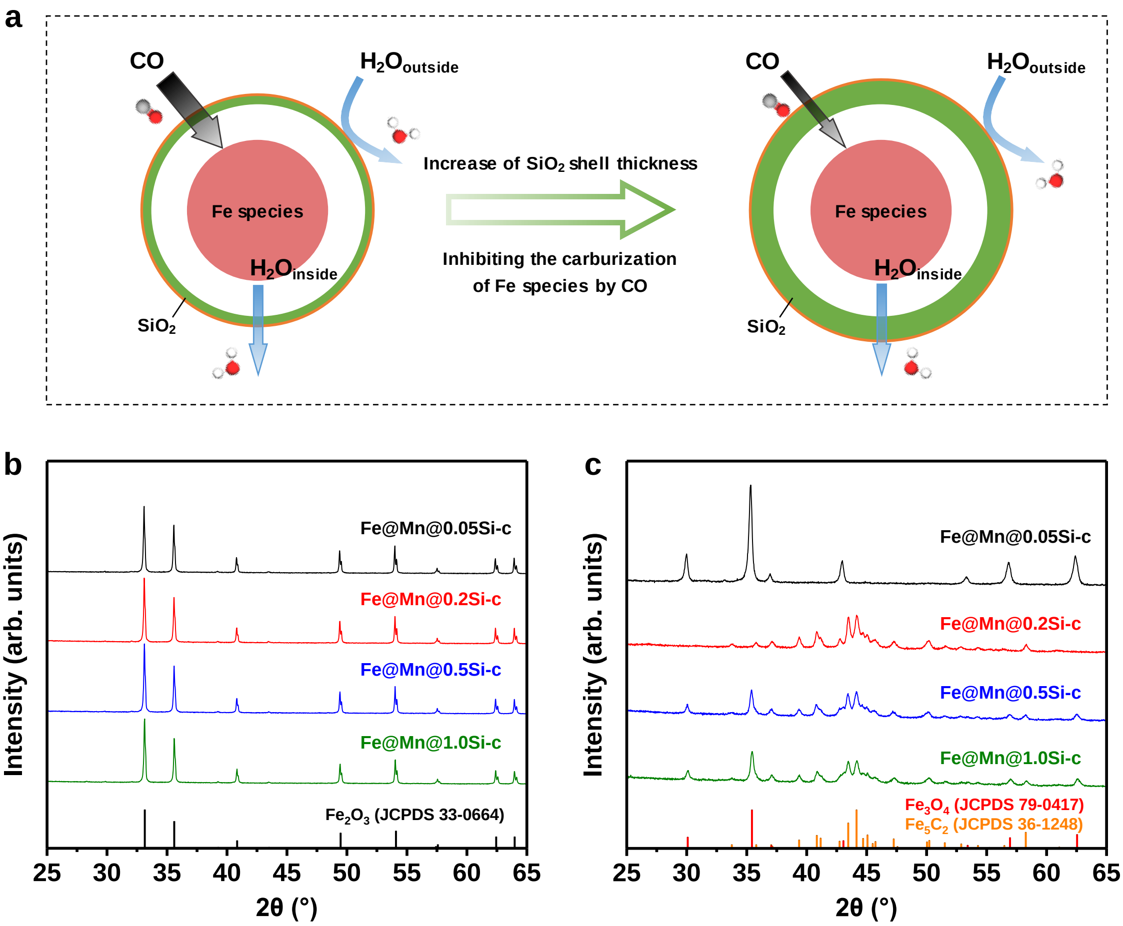

Supplementary Fig. 17. (a) Diffusion model of CO and H_2O on the hydrophobic catalysts during the FTS reaction. XRD patterns of the (b) fresh and (c) spent catalysts.

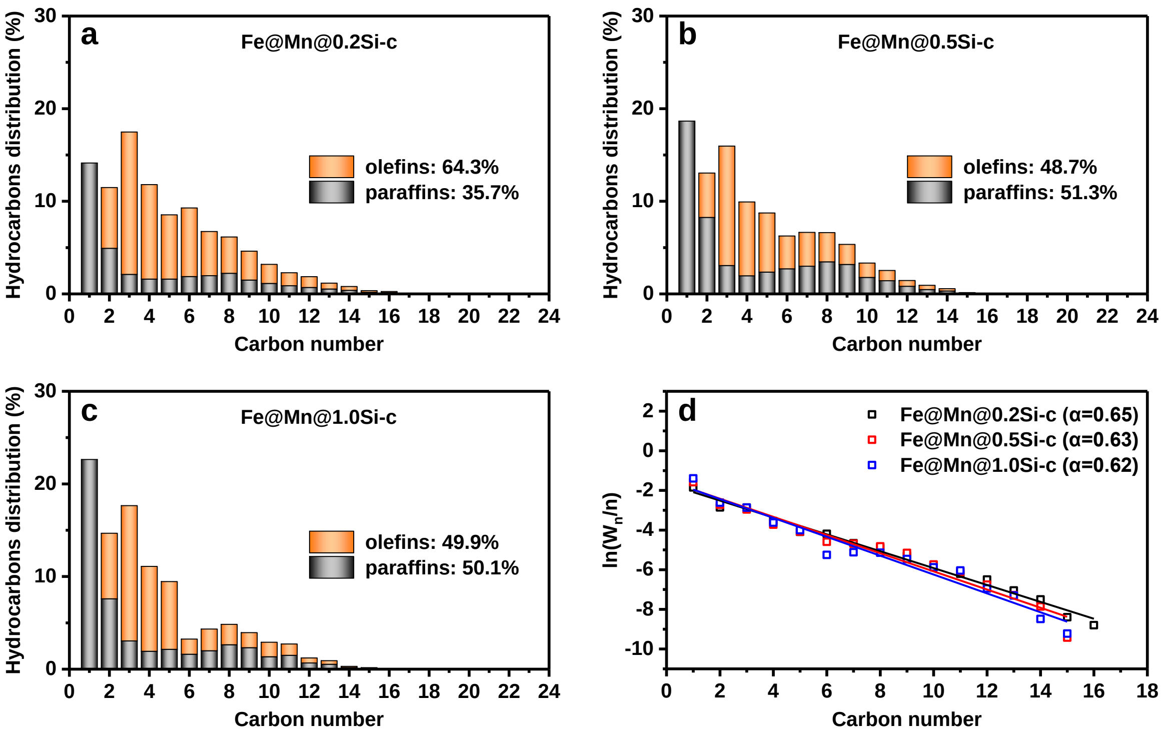

Supplementary Fig. 18. Hydrocarbons distribution of the (a) Fe@Mn@0.2Si-c, (b) Fe@Mn@0.5Si-c, and (c) Fe@Mn@1.0Si-c catalysts. (d) The ASF plots and relevant chain growth probability (α value) of the Fe@Mn@*x*Si-c catalysts.

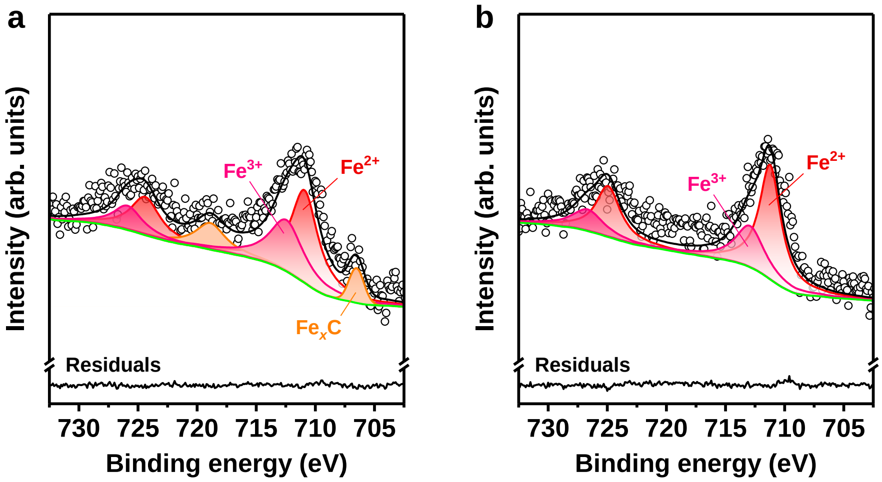

Supplementary Fig. 19. XPS spectra of Fe 2*p* on the spent (a) Fe@Mn@0.05Si and (b) Fe@Mn@0.05Si-c catalysts.

After reaction, a peak at 706.5 eV appeared on the spent Fe@Mn@0.05Si catalyst, which was attributed to the Fe_xC species[4,5]. As for the spent Fe@Mn@0.05Si-c catalyst, no peak related to the Fe_xC species was detected, suggesting that no iron carbide existed on the surface layer of this catalyst.

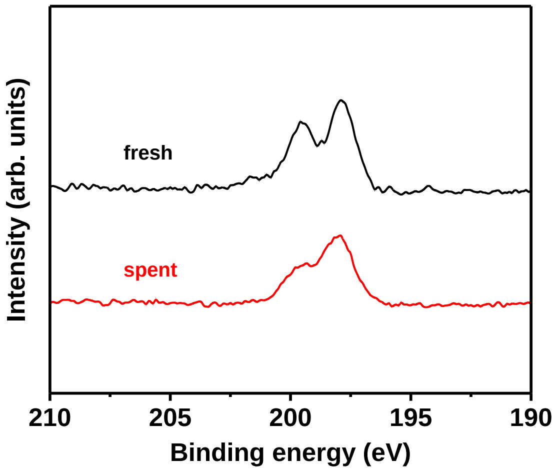

Supplementary Fig. 20. XPS spectra of Cl 2*p* on the fresh and spent Fe@Mn-c catalysts.

Chlorine strongly adsorbed on the catalyst surface, and it still existed stably on the Fe@Mn-c catalyst after reaction.

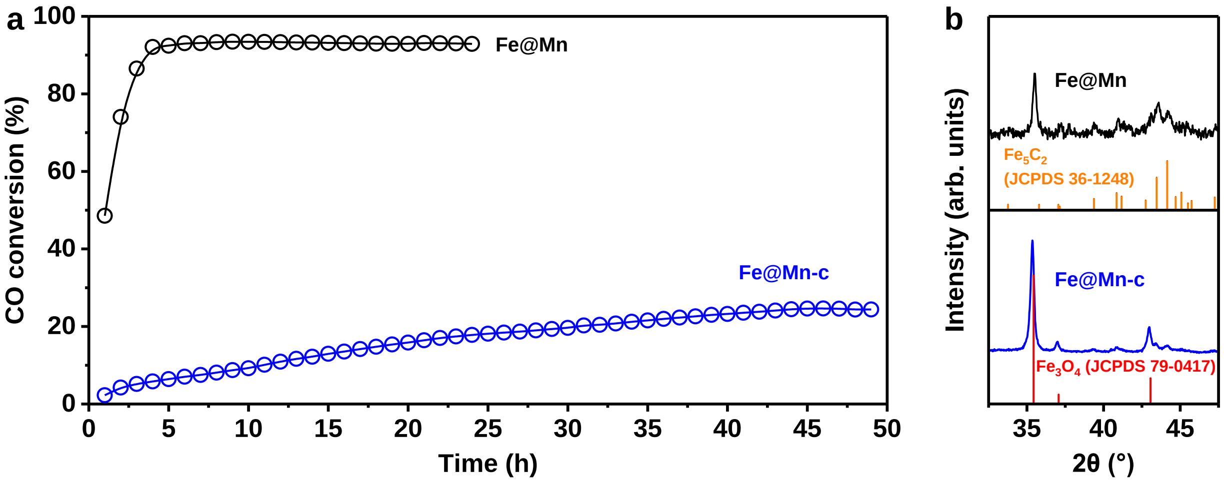

Supplementary Fig. 21. (a) CO conversion on the Fe@Mn and Fe@Mn-c catalysts with time on stream. (b) XRD patterns of the spent Fe@Mn and Fe@Mn-c catalysts.

Chlorine existed stably on the surface of the Fe@Mn-c catalyst during reaction (Supplementary Fig. 20), and it suppressed the formation of Fe_xC active phase (Supplementary Fig. 21b). As a result, the Fe@Mn-c catalyst exhibited a much lower CO conversion than the Fe@Mn catalyst without chlorine (Supplementary Fig. 21a). These results further confirmed that the existence of chlorine on catalyst surface could obviously reduce the catalytic activity of catalyst.

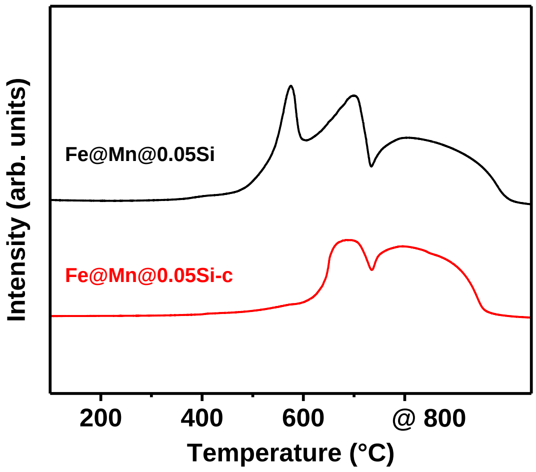

Supplementary Fig. 22. H_2-TPR profiles of catalysts.

Compared with the Fe@Mn@0.05Si catalyst, the reduction peaks of the Fe@Mn@0.05Si-c catalyst shifted towards much higher temperature and the peaks area decreased obviously, suggesting that the residual chlorine on catalyst inhibited notably the reduction process of iron species by H_2 molecules.

Supplementary Table 1. Elemental analysis of the Fe@Mn@*x*Si catalysts.

Catalyst	Parameters of catalyst preparation		Content in catalyst (wt.%) [a]		
	Dosage of Fe@Mn	Dosage of TEOS	Mn	Si	SiO_2
Fe@Mn	0.5 g	0 mL	6.1	0.2	0.3
Fe@Mn@0.05Si	0.5 g	0.05 mL	6.5	1.3	2.7
Fe@Mn@0.2Si	0.5 g	0.2 mL	5.9	4.1	8.8
Fe@Mn@0.5Si	0.5 g	0.5 mL	5.8	5.7	12.1
Fe@Mn@1.0Si	0.5 g	1.0 mL	4.2	11.6	24.9
Fe@Mn@2.8Si	0.5 g	2.8 mL	4.4	15.8	34.0

[a] The contents of Mn and Si in the Fe@Mn@*x*Si catalysts were determined by ICP.

Supplementary Table 2. Calculation of the relative spatial size of different iron phases.

Iron phase	V_0 (Å^3) [a]	n_{Fe} [b]	V (Å^3) [c]	Relative spatial size [d]
Fe_2O_3	301.3	12	3012.8	100.0%
Fe_3O_4	575.9	24	2879.7	95.6%
Fe_5C_2	266.0	20	1595.9	53.0%
Fe_3C	154.6	12	1546.2	51.3%

[a] Volume of unit cell.

[b] Number of Fe atom in unit cell.

[c] Volumes of different iron phases with 120 Fe atoms.

[d] The volume ratios of different iron phases to Fe_2O_3 phase with the same number of Fe atoms.

Supplementary Table 3. Detailed Mössbauer parameters.

Catalyst	Assignment	Mössbauer parameters			
		IS (mm/s)	QS (mm/s)	Hhf (kOe)	Spectral contribution (%)
Fe@Mn@0.2Si	Fe^{3+} (spm)	0.37	0.97	/	6.0
	Fe_3O_4 (A)	0.30	-0.02	492	18.4
	Fe_3O_4 (B)	0.63	-0.05	457	15.9
	χ-Fe_5C_2 (I)	0.24	-0.09	219	23.9
	χ-Fe_5C_2 (II)	0.18	-0.03	182	23.6
	χ-Fe_5C_2 (III)	0.18	-0.15	108	12.2
Fe@Mn@0.2Si-c	χ-Fe_5C_2 (I)	0.23	-0.08	212	36.9
	χ-Fe_5C_2 (II)	0.19	0.03	179	15.5
	χ-Fe_5C_2 (III)	0.20	0.03	111	21.7
	θ-Fe_3C	0.19	0.00	198	25.9

Supplementary References

[1] Zhang, C., Wan, H., Yang, Y., Xiang, H. & Li, Y. Study on the iron–silica interaction of a co-precipitated Fe/SiO_2 Fischer–Tropsch synthesis catalyst. *Catal. Commun.* **7**, 733–738 (2006).

[2] Yao, D. et al. A high-performance nanoreactor for carbon–oxygen bond hydrogenation reactions achieved by the morphology of nanotube-assembled hollow spheres. *ACS Catal.* **8**, 1218–1226 (2018).

[3] Yao, D. et al. Balancing effect between adsorption and diffusion on catalytic performance inside hollow nanostructured catalyst. *ACS Catal.* **9**, 2969–2976 (2019).

[4] Zhai, P. et al. Highly tunable selectivity for syngas-derived alkenes over zinc and sodium-modulated Fe_5C_2 catalyst. *Angew. Chem. Int. Ed.* **55**, 9902–9907 (2016).

[5] Zhu, J. et al. Dynamic structural evolution of iron catalysts involving competitive oxidation and carburization during CO_2 hydrogenation. *Sci. Adv.* **8**, eabm3629 (2022).